Confinement effects in premelting dynamics

Satyajit Pramanik[*]

Nordita, Royal Institute of Technology and Stockholm University, Stockholm, Sweden

John S. Wettlaufer[†]

Yale University, New Haven, Connecticut, USA;
Mathematical Institute, University of Oxford, Oxford, UK;
and Nordita, Royal Institute of Technology and Stockholm University, Stockholm, Sweden

We examine the effects of confinement on the dynamics of premelted films driven by thermomolecular pressure gradients. Our approach is to modify a well-studied setting in which the thermomolecular pressure gradient is driven by a temperature gradient parallel to an interfacially premelted elastic wall. The modification treats the increase in viscosity associated with the thinning of films, studied in a wide variety of materials, using a power law and we examine the consequent evolution of the confining elastic wall. We treat (1) a range of interactions that are known to underlie interfacial premelting and (2) a constant temperature gradient wherein the thermomolecular pressure gradient is a constant. The difference between the cases with and without the proximity effect arises in the volume flux of premelted liquid. The proximity effect increases the viscosity as the film thickness decreases thereby requiring the thermomolecular pressure driven flux to be accommodated at higher temperatures where the premelted film thickness is the largest. Implications for experiment and observations of frost heave are discussed.

I. INTRODUCTION

A host of phenomena extend the equilibrium domain of one phase into the bulk region of a neighboring phase. In general, such an extension is associated with effective surface fields—forces that are extensive with area even when their underlying origins are volume-volume interactions. Examples include, among many others, van der Waals and screened Coulomb interactions or steric effects, e.g., [1–4]. Here we focus on *premelting*, wherein a solid-wall or solid-vapor interface is wet by the melt phase of the solid in equilibrium due to the relative polarizabilities of a solid-liquid-wall (*interfacial premelting*) or solid-liquid-vapor (*surface melting*) interface. One prepares the "dry" solid-wall or solid-vapor interface at a pressure and temperature below the bulk melting transition and approaching the latter from below. If the interface is wet by the melt phase then, depending on the detailed nature of the underlying interactions, the film will become arbitrarily thick as the bulk transition is approached.

Here we focus upon interfacial premelting, which, as in the case of surface melting, occurs on at least one facet of most materials [5] and has been thoroughly studied for a wide class of wall materials (conductors, dielectrics, and polymers) in the case of ice [6]. The liquid film (l) has a thickness d and disjoins the solid phase (s) from a wall at temperatures below the bulk freezing point T_m. The mean-field description of the system has a grand potential

$$\Omega = -P_l V_l - P_s V_s + \mathcal{I}(d). \qquad (1)$$

Here P and V denote pressure and volume, and the volume-volume interactions are captured by the part of free energy $\mathcal{I}(d) = [\Delta\sigma f(d) + \sigma_{\text{sw}}]A_i$ that is extensive with interfacial area A_i, where $\Delta\sigma = \sigma_{\text{sl}} + \sigma_{\text{lw}} - \sigma_{\text{sw}}$, and the σ's are the

solid-liquid (sl), liquid-wall (lw), and solid-wall (sw) interfacial free energies [7]. Thus, when the dry interfacial energy, σ_{sw}, is larger than $\sigma_{\text{sl}} + \sigma_{\text{lw}}$, then sufficient conditions for the interface to be wet by the melt are met. Power-law interaction potentials have the form $f(d) = 1 - (d_0/d)^{-n+1}$, where d_0 is on the order of a molecular diameter, and n depends on the nature of the interactions attracting the melt liquid to the solid, for example, $n = 3$ ($n = 4$) corresponds to nonretarded (retarded) van der Waals interactions. Minimizing Ω at fixed temperature, close to the bulk melting temperature T_m, total volume, and chemical potential yields the film thickness

$$d = \left[-\frac{(n-1)d_0^{n-1}\Delta\sigma}{\rho_l q_m} \right]^{1/n} t_r^{-1/n} \equiv \lambda_n t_r^{-1/n}, \qquad (2)$$

where $t_r = (T_m - T)/T_m$ is the reduced temperature, ρ_l is the liquid density, and q_m is the latent heat of fusion [7,8]. Moreover, the interfacial interactions create a pressure difference between the melted layer and the bulk solid [7,8],

$$P_l - P_s = \Delta\sigma(n-1)d_0^{n-1}d^{-n}, \qquad (3)$$

akin to the disjoining pressure of wetting dynamics, e.g., [9]. Combining Eqs. (2) and (3), a universal thermodynamic expression—independent of the nature of the interactions—lays bare the essential idea of premelting dynamics, viz.,

$$P_l = P_s - \rho_l q_m t_r. \qquad (4)$$

We fix P_s by making contact with a reservoir and impose a temperature gradient parallel to the premelted surface. Therefore, as seen from Eq. (4), P_l increases with temperature and drives a flow in the film toward lower temperatures. Now, Eq. (2) shows that the film thickness is a unique function of temperature and hence conservation of mass demands that a gradient in the volume flux must convert any liquid in excess of that value into a solid as the liquid flows toward lower temperatures as shown in Fig. 1.

———————
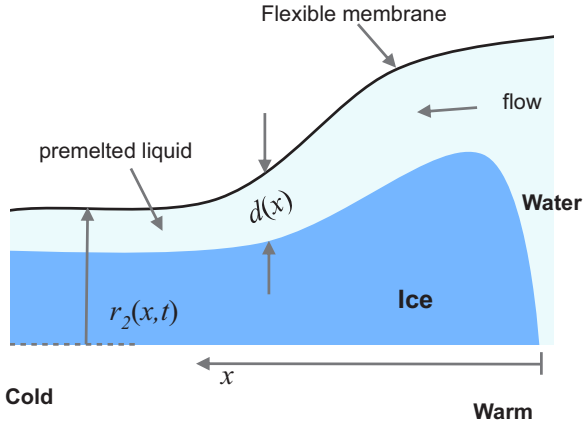[*]satyajit.math16@gmail.com
[†]john.wettlaufer@yale.edu

FIG. 1. Schematic of the flow of a premelted film disjoining an elastic capillary tube from the solid phase, from [10].

The basic dynamics of premelted films has been studied quantitatively in the case of ice, both at single crystal interfaces and in porous media, in part because of its geophysical implications [5,8,10–12], particularly in frost heave. It has also been studied in argon [13], benzene [14], and helium [15], which contract upon solidification.

II. CONFINEMENT EFFECTS

Liquids confined between solids of other materials behave differently than their bulk counterparts. For example, as a confined liquid approaches a thickness of a handful of molecular layers, the bulk melting and freezing transitions vanish and molecular mobilities take values intermediate between those found in a bulk solid or bulk liquid [1,16,17]. Molecular hydrodynamics show a layering normal to walls that depends on the nature of the wall-fluid interactions, but the influence on rheology is complex, ranging from shear thinning to shear thickening, so that new dynamical behavior emerges when a liquid is confined in a narrow gap [18].

The dynamical consequences of the basic issue of how a premelted interface transitions from a disordered solid to a bulk liquid as the temperature increases is worth examining quantitatively. Equation (2) shows that as the temperature becomes arbitrarily small, the film becomes arbitrarily thin. Clearly, the concept of a bulk liquid will break down at thicknesses greater than the value of d_0, with the detailed nature of the breakdown depending on the material under consideration. As the film thins, the ordering imposed on the liquid by the solid may eventually span the interfacially melted gap, imprinting properties that are intermediate between a liquid and a solid. For example, when transecting the bulk ice-water interface from the solid side, the density and diffusivity transition from the bulk solid to the bulk liquid values over tens of angstroms, depending on crystallographic orientation of the solid and the degree of disequilibrium (e.g., [19–21] and references therein). Hence, we expect that as the temperature of a premelted film decreases, such structural changes may have dynamical consequences. For example, Pittenger et al. [22] have shown that the viscosity of quasiliquid water on ice can be several orders of magnitude larger than the bulk value, which may also influence the kinetic friction of ice surfaces [23,24]. However,

whereas premelting dynamics have been studied in some detail for ice surfaces, confinement effects on dynamical properties have been more thoroughly studied in other materials.

The flow of confined liquids cannot be understood by simple extrapolation of the bulk properties. A number of experimental studies have focused on the viscosity of nanometer-scale liquid films. For example, in experiments wherein a thin film of water of nanometer scale is confined between different surfaces, Dhinojwala and Granick [25] and Major et al. [26] have shown that the effective viscosity of the confined water ($\eta_{\text{eff}} \approx 3 \times 10^4$ Pa s) is approximately 10^7 times larger than the bulk viscosity of water ($\eta_{\text{bulk}} = 8.6 \times 10^{-4}$ Pa s). Bureau [27] has shown that the effective viscosity of octamethylcyclotetrasiloxane (OMCTS) confined in molecularly thin films can increase from the bulk value by approximately 10^2. Moreover, the effective viscosity increased with the number of molecular layers as a power law. On the other hand Raviv and Klein [28] conclude from their shear experiments that surface-bound aqueous salt solutions retain bulk characteristics even when compressed to nanometer scales.

Granick [29] showed experimentally that the effective viscosity of a simple confined molecular liquid (dodecane) appears to diverge as the thickness decreases under 40 nm. Zhu and Granick [30] measured a confinement enhancement of the viscosity of OMCTS between mica sheets by two orders of magnitude as the sheet distance decreased by 14 nm. Zhu and Granick [31] measured a confinement enhancement of the viscosity of alkane fluids between mica sheets by two orders of magnitude (factors of 5–6) as sheet distance decreased by 6 nm under quasisteady (rapid) quenching. Besides the rate, an important factor in such experiments is the degree of perfection of the mica surfaces.

In summary, while the experimental setting spans a range of materials and confining surfaces, it provides a conceptual framework for treating the dynamical consequences of the enhanced solid-like structure as premelted films thin in terms of an enhancement of the viscosity of the layer. Such an enhancement will suppress the volume flux under thermomolecular pressure gradients, thereby changing the solidification process shown schematically in Fig. 1, at least as the flow extends into low temperatures.

We understand the dynamics of premelted ice surfaces from theoretical and experimental studies of solidification in elastic capillary tubes [7] and disks [8]. Here, we revisit the capillary tube problem using a proposed general power-law relation for the dynamic viscosity of the melt liquid with the film thickness as

$$\eta(d) = \eta_0 - (\eta_0 - \eta_b)\left[1 - \left(\frac{d_0}{d}\right)^\gamma\right], \qquad (5)$$

where $\gamma > 0$ such that $\eta(d) \to \eta_b$ (bulk viscosity) as $d \to \infty$, and $\eta(d) \to \eta_0$ when $d \to d_0^+$, and the continuum approximation breaks down. In order to generate a sense of the range of γ for a given value of $\eta_r = \eta_0/\eta_b$, we perform a linear least-squares fit of this model for two sets of experimental data (Fig. 2). This is preferred to fitting the confinement enhanced viscosity data from many individual experiments, such as those described above, for which we may have no information regarding the phenomenon of interfacial premelting. We
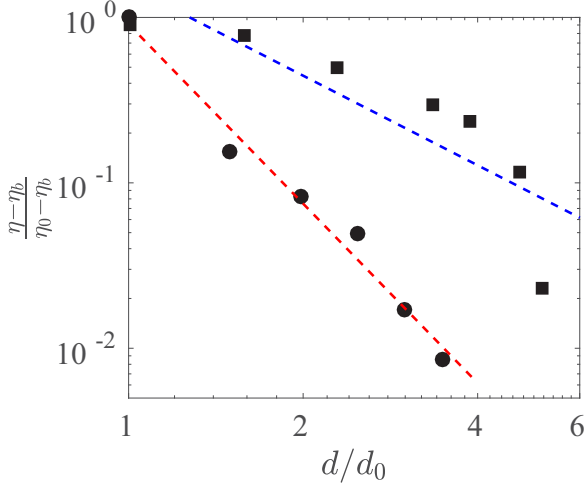
FIG. 2. Least-squares fit (dashed lines) of $(\eta - \eta_b)/(\eta_0 - \eta_b) = \beta(d_0/d)^\gamma$ to the experimentally measured viscosity (filled symbols) from [32] (circles; OMCTS), giving $\beta = 0.91, \gamma = 3.60$ and [31] (squares; squalane), giving $\beta = 1.55, \gamma = 1.80$.

believe this avoids the risks associated with the introduction of more specific detail than can be justified by firm evidence.

III. SOLIDIFICATION IN A CAPILLARY TUBE

Within the framework of a mathematical model we have previously studied the dynamics of premelted films in a capillary tube with elastic walls [7]. Here we modify this theory by incorporation of the confinement effect through Eq. (5), but in order to make our treatment reasonably self-contained we outline the main steps in the development of the key dynamical equation presently.

As shown in Fig. 1 and described when discussing Eq. (4), a temperature gradient that is imposed parallel to the premelted surface will create a flow driven by a thermomolecular pressure gradient,

$$\nabla P_l = -\rho_l q_m \nabla t_r + \frac{\rho_l}{\rho_s} \nabla P_s, \quad (6)$$

where P_s is the membrane-exerted external pressure on the solid. Mass conservation in the thin film of thickness $d = r_2 - r_1$, between the solid of radius r_1 and the capillary tube of radius r_2, is

$$\partial_t\left(\pi r_2^2\right) + \partial_x Q = 0, \quad (7)$$

where Q is the volume flux, which for an annular lubrication flow through the film is

$$Q = -\frac{\pi}{6}\frac{r_2 d^3}{\eta}\left(\frac{\rho_l}{\rho_s}\partial_x P_s - \rho_l q_m \partial_x t_r\right). \quad (8)$$

Here, $\eta = \eta(d)$ is the dynamic viscosity of the melt given by Eq. (5), and, as previously [7], we assume that the capillary wall exerts a linear elastic hoop stress upon the solid given by

$$P_s = k(r_2 - r_0), \quad (9)$$

where k is a constant and r_0 is the undeformed radius, viz., $r_2(x,t=0) = r_0(x)$.

For constant bulk viscosity in the case of both transient and steady-state thermal fields, similarity solutions of the capillary

radius were obtained [7], but here we are interested in the latter case and thus take a constant temperature gradient $\mathcal{G}$, such that the reduced temperature is $t_r = \mathcal{G}x/T_m$. Thus, in this temperature field, using Eq. (2) in Eq. (5), the dynamic viscosity becomes a function of position, viz.,

$$\eta(x) = \eta_0 - (\eta_0 - \eta_b)\left[1 - \left\{\frac{d_0}{\lambda_n}\left(\frac{\mathcal{G}}{T_m}\right)^{1/n}\right\}^\gamma x^{\gamma/n}\right], \quad (10)$$

and combined with Eqs. (7)–(9), mass conservation can be written solely in terms of the capillary radius as

$$\partial_t r_2 - \frac{\rho_l k \lambda_n^3}{12\rho_s}\left(\frac{T_m}{\mathcal{G}}\right)^{3/n}\partial_x\left[\frac{x^{-3/n}}{\eta(x)}\partial_x\left(r_2 - r_0 - \frac{\rho_s q_m \mathcal{G}}{k T_m}x\right)\right]$$
$$= 0. \quad (11)$$

Whence, the capillary deformation can be obtained by solving Eq. (11) subject to the following boundary and initial conditions:

$$r_2 - r_0 = 0 \ (x = 0) \quad \text{and} \quad r_2 - r_0 = 0 \ (x \to \infty), \quad (12a)$$

$$r_2(x,t = 0) = r_0(x), \quad (12b)$$

and

$$\partial_x(r_2 - r_0) = \frac{\rho_s q_m \mathcal{G}}{k T_m} \ (x = 0), \quad (12c)$$

Equations (12a) express no deformation at the bulk solid-liquid interface and as $d \to d_0^+$, while Eq. (12c) is a necessary condition to remove the singularity at $x = 0$.

A. Nondimensionalization

We render the above system of equation dimensionless with the following scaling:

$$\tilde{x} = \frac{x}{X_0}, \quad \tilde{t} = \frac{t}{X_0^{2+3/n}/\Gamma_n}, \quad \tilde{r} = \frac{r_2 - r_0}{\alpha X_0}, \quad (13a)$$

$$\tilde{\eta}(\tilde{x}) = \frac{\eta_0 - \eta}{\eta_0 - \eta_b} = \left[1 - \left\{\frac{d_0}{\lambda_n}\left(\frac{\mathcal{G}X_0}{T_m}\right)^{1/n}\right\}^\gamma \tilde{x}^{\gamma/n}\right]$$
$$= [1 - d_{\gamma,n}\tilde{x}^{\gamma/n}], \quad (13b)$$

wherein

$$\Gamma_n = \frac{\rho_l k \lambda_n^3}{12\eta_b \rho_s}\left(\frac{T_m}{\mathcal{G}}\right)^{3/n}, \quad \alpha = \frac{\rho_s q_m \mathcal{G}}{k T_m}, \quad (14)$$

from which we obtain

$$\partial_{\tilde{t}}\tilde{r} + \partial_{\tilde{x}}\left[-\frac{\tilde{x}^{-3/n}}{\eta_1(\tilde{x})}(\partial_{\tilde{x}}\tilde{r} - 1)\right] = 0, \quad (15a)$$

$$\eta_1(\tilde{x}) = \eta_r - (\eta_r - 1)\tilde{\eta}(\tilde{x}) = 1 + (\eta_r - 1)d_{\gamma,n}\tilde{x}^{\gamma/n}, \quad (15b)$$

$$\tilde{r} = 0 \ (\tilde{x} = 0, 1), \quad (15c)$$

$$\tilde{r} = 0 \ (\tilde{t} = 0), \quad (15d)$$

$$\partial_{\tilde{x}}\tilde{r} - 1 = 0. \quad (15e)$$

Here, X_0 is a length scale chosen based on the temperature gradient. For clarity of notation, the dimensionless variables are now denoted without the tilde overscripts, except when time, t appears in combination with Γ_n or otherwise specified.

We discuss the dimensional variables explicitly in concert with their SI units.

Expanding the flux gradient, $\partial_x \mathcal{Q} \equiv \partial_x [-\frac{x^{-3/n}}{\eta_1(x)}(\partial_x r - 1)]$, we rewrite Eq. (15a) in the form of an advection-diffusion equation with a source, $\mathcal{F}_n(x)$, as

$$\partial_t r = \mathcal{D}_n(x)\partial_{xx} r + \mathcal{U}_n(x)\partial_x r + \mathcal{F}_n(x), \quad (16)$$

in which

$$\mathcal{D}_n(x) = \frac{x^{-3/n}}{\eta_1(x)} > 0, \quad (17a)$$

$$\mathcal{U}_n(x) = -\frac{x^{-(1+3/n)}}{\eta_1^2(x)}\left[\left(\frac{3}{n} + \frac{\gamma}{n}\right)\eta_1(x) - \frac{\gamma}{n}\right] < 0, \quad (17b)$$

$$\mathcal{F}_n(x) = \frac{x^{-(1+3/n)}}{\eta_1^2(x)}\left[\left(\frac{3}{n} + \frac{\gamma}{n}\right)\eta_1(x) - \frac{\gamma}{n}\right] > 0. \quad (17c)$$

A key difference between the previous treatment [7] and the one here is that the proximity effect, treated through the viscosity model of Eq. (15b), introduces an inhomogeneity so that Eq. (16) does not have a general similarity solution. However, we note that for $\eta_1(x) = 1$ [i.e., $\eta = \eta_b$, from Eqs. (13b) and (15b)], Eq. (11) simplifies to

$$\partial_t r_2 + \Gamma_n \partial_x [x^{-3/n}\{\alpha - \partial_x (r_2 - r_0)\}] = 0, \quad (18)$$

which is satisfied by the similarity solution,

$$r_2 - r_0 = \alpha(\Gamma_n t)^{n/(2n+3)} g(\zeta), \quad (19)$$

with similarity variable

$$\zeta = x(\Gamma_n t)^{-n/(2n+3)}. \quad (20)$$

One obtains the similarity solution $g(\zeta)$ by solving a boundary value problem of a family of second-order, ordinary differential equations,

$$g - \zeta g' = \left(2 + \frac{3}{n}\right)[\zeta^{-3/n}(g' - 1)]', \quad (21a)$$

$$g = 0 \ (\zeta = 0) \quad \text{and} \quad g \to 0 \ (\zeta \to \infty), \quad (21b)$$

where the primes denote $d/d\zeta$, supplemented by the necessary condition

$$g' = 1 \ (\zeta = 0) \quad (22)$$

that there is no singularity at the bulk solid-liquid interface.

IV. RESULTS

A. Analytical results

Approximation of $\gamma_{\text{crit}}(\eta_r, d_0, n)$ and $\gamma_{\text{sat}}(\eta_r, d_0, n)$

Clearly, the nature of the solution to Eq. (16) depends on the proximity effect embodied in the behavior of $\eta_1(x)$. For example, we obtain the similarity solution (19) either for $\eta_r = 1$ or when $\eta_1(x) = 1 + (\eta_r - 1)d_{\gamma,n}x^{\gamma/n} \sim O(1)$, for all x, and $\gamma \geqslant \gamma_{\text{sat}}(\eta_r, d_0, n)$. Here, the subscript 'sat' denotes saturation of the viscosity, $\eta(d)$, to the bulk viscosity, η_b.

Now, we estimate $\gamma_{\text{sat}}(\eta_r, d_0, n)$ and $\gamma_{\text{crit}}(\eta_r, d_0, n)$ (described below) from $\eta_1(x)$. For $0 \leqslant x \leqslant 1$, when $\eta_r d_{\gamma,n} \sim O(1)$, then

$$1 + (\eta_r - 1)d_{\gamma,n}x^{\gamma/n} \sim O(1), \quad (23)$$

which yields

$$\gamma_{\text{sat}}(\eta_r, d_0, n) = -\frac{\ln \eta_r}{\ln(d_0/\lambda_n) + \ln(\mathcal{G}X_0/T_m)/n}. \quad (24)$$

On the other hand, when $\eta_1(x) = 1 + (\eta_r - 1)d_{\gamma,n}x^{\gamma/n} \sim O(x^{\gamma/n})$, $\forall x$, the capillary deformation is given by

$$g_\gamma - \zeta_\gamma g'_\gamma = \left(2 + \frac{3-\gamma}{n}\right)\left[\zeta_\gamma^{-\frac{3-\gamma}{n}}(g'_\gamma - 1)\right]'. \quad (25)$$

Subject to the conditions in Eqs. (21b) and (22), the ordinary differential equation (25) has the following similarity solution

$$g_\gamma(\zeta_\gamma) = (r_2 - r_0)\alpha^{-1}\left[\frac{\Gamma_n t}{(\eta_r - 1)d_{\gamma,n}}\right]^{-n/(2n+3+\gamma)}, \quad (26)$$

with similarity variable

$$\zeta_\gamma = x\left[\frac{\Gamma_n t}{(\eta_r - 1)d_{\gamma,n}}\right]^{-n/(2n+3+\gamma)}. \quad (27)$$

When $\eta_1(x) = 1 + (\eta_r - 1)d_{\gamma,n}x^{\gamma/n}$ exhibits both $O(1)$ and $O(x^{\gamma/n})$ behaviors locally in $0 \leqslant x \leqslant 1$, there is a length scale imposed upon the system, which preempts the existence of a similarity solution. One can show that

$$1 + (\eta_r - 1)d_{\gamma,n}x^{\gamma/n} \sim O(1), \quad \text{at } x = 0^+, \quad (28)$$

and

$$1 + (\eta_r - 1)d_{\gamma,n}x^{\gamma/n} \sim O(x^{\gamma/n}), \quad \text{for } x > 0^+, \quad (29)$$

when $\eta_r d_{\gamma,n}\epsilon^{\gamma/n} \sim O(1)$ for $0 < \epsilon \ll 1$, which yields

$$\gamma_{\text{crit}}(\eta_r, d_0, n) = -\frac{\ln \eta_r}{\ln(d_0/\lambda_n) + [\ln(\mathcal{G}X_0/T_m) + \ln \epsilon]/n}. \quad (30)$$

When the solution of Eq. (15a) for the proximity viscosity model with $\gamma \in (\gamma_{\text{crit}}, \gamma_{\text{sat}})$ intersects the solution corresponding to the bulk viscosity model at $x = x_{\text{cross}}$, then, upon substitution of $\epsilon = x_{\text{cross}}$ into Eq. (30), one obtains the corresponding value of γ. Since we have no *a priori* information about x_{cross}, we cannot provide an analytic expression for it. However, we can use numerical solutions to compute x_{cross} *a posteriori*. Thus, one obtains γ_{sat} from γ_{crit} in the limit $\epsilon \to 1$.

Taking the limit $\gamma \to 0^+$, $\eta \to \eta_0$ in Eq. (13b), the viscosity of the liquid film is independent of the film thickness. This is analogous to the previous model [7], but with the viscosity increased by a factor η_r, and we obtain the similarity solution

$$g_{\gamma\to 0^+} = (r_2 - r_0)\alpha^{-1}\left(\frac{\Gamma_n t}{\eta_r}\right)^{-n/(2n+3)} = g(\zeta)\eta_r^{n/(2n+3)}, \quad (31)$$

with similarity variable

$$\zeta_{\gamma\to 0^+} = x\left(\frac{\Gamma_n t}{\eta_r}\right)^{-n/(2n+3)} = \zeta\eta_r^{n/(2n+3)}, \quad (32)$$

which satisfies Eqs. (21a) and (21b), and the necessary condition (22).

B. Numerical results

We discretized Eq. (16) using the standard second-order finite difference formulas and integrate in time using the
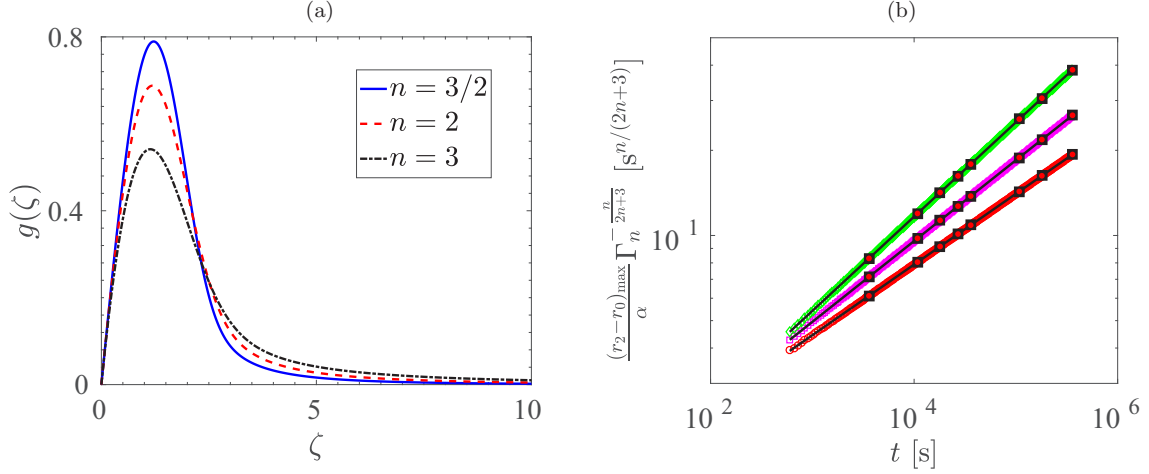
FIG. 3. (a) Similarity solution, Eq. (19), for the short- and long-range electrostatic ($n = 3/2$ and $n = 2$) and nonretarded van der Waals ($n = 3$) interactions. (b) For each type of interaction (i.e., each n), a linear least-squares fit gives a power-law relation for the maximum capillary deformation, $(r_2 - r_0)_{\max}(t) \propto t^{n/(2n+3)}$, as given by Eq. (19). The $t^{1/4}$, $t^{2/7}$, and $t^{1/3}$ power laws are for $n = 3/2$ (lower curve), $n = 2$ (middle curve), and $n = 3$ (upper curve) respectively. The solid lines correspond to $g_{\max,n} t^{n/(2n+3)}$ and the filled symbols correspond to the parameters for dodecane for $d_0 = 1$ Å (black squares) and $d_0 = 10$ Å (solid dots). Note, in (b) t denotes dimensional time.

semi-implicit Crank-Nicolson method [33,34]. We use uniform grid spacing Δx and Δt for the space and time, respectively (see the Supplemental Material for the numerical scheme [35]).

The similarity solution, Eq. (19), is constructed from the numerical solution of Eq. (16) for the bulk viscosity model and is plotted in Fig. 3(a) for the short- and long-range electrostatic ($n = 3/2$ and $n = 2$) and nonretarded van der Waals ($n = 3$) interactions. The self-similar structure of the solution is obtained with $g_{\max,3} \approx 0.5415$ at $\zeta_{\max,3} \approx 1.1341$; $g_{\max,2} \approx 0.6877$ at $\zeta_{\max,2} \approx 1.1853$, and $g_{\max,3/2} \approx 0.7894$ at $\zeta_{\max,3/2} \approx 1.2162$. From Eqs. (13a), (19), and (20), it can be shown that $(r_2 - r_0)_{\max} = \alpha g_{\max,n} \Gamma_n^{n/(2n+3)} t^{n/(2n+3)}$. Furthermore, to demonstrate the robustness of the numerical method used, we calculated $(r_2 - r_0)_{\max} \alpha^{-1} \Gamma_n^{-n/(2n+3)}$ as a function of dimensional time from the numerical solutions, which are plotted in Fig. 3(b). For any given n, the scaling behavior of the similarity solution is independent of the molecular diameter (d_0) and λ_n. In other words, the similarity solution is characterized by a single parameter, n. For the nonretarded van der Waals interactions ($n = 3$), we recover the results of Wettlaufer and Worster [7] [see their Eqs. (51)–(56)].

The results from the numerical computations presented below were obtained using a temperature gradient of $\mathcal{G} = 1$ K/m (or 10^2 K/m), a final (dimensional) time of integration $T_f = 10^2$ h, and (a) $n = 3$, $\eta_r = 10^2, 10^3, 10^4, 10^5, 10^6, 10^7$, $d_0 = 8$ Å, $\lambda_3 = 5.3947$ Å; (b) $n = 2$, $\eta_r = 10^7$, $d_0 = 8$ Å, $\lambda_2 = 5.3947$ Å. The explored range of the power-law exponent γ is tabulated in the Appendix.

1. $\gamma_{\mathrm{crit}}(\eta_r, d_0, n)$ and $\gamma_{\mathrm{sat}}(\eta_r, d_0, n)$

For given values of γ, η_r, d_0, and n (hence λ_n), we compute the maximum deformation, $r_{\max}(t; \gamma, \eta_r, d_0, n)$, as a function of time, t. For each γ, a linear least-squares fit is used to obtain

a power law:

$$r_{\max}(t; \gamma, \eta_r, d_0, n) = a(\gamma, \eta_r, d_0, n) t^{b(\gamma, \eta_r, d_0, n)}. \quad (33)$$

Figure 4 shows $b(\gamma, \eta_r, d_0, n)$ for $\eta_r = 10^7, d_0 = 8$ Å, and $n = 3$ along with the exponents $n/(2n + 3)$ and $n/(2n + 3 + \gamma)$ of the two similarity solutions (19) and (26), respectively. We show that $b(\gamma, \eta_r, d_0, n)$ coincides with $n/(2n + 3 + \gamma)$ for $0 < \gamma \lesssim 2.75$, and with $n/(2n + 3)$ for $\gamma \gtrsim 6.25$. This is in accordance with our analytical argument above concerning the existence of two different similarity solutions depending upon the power-law exponent γ. For a more quantitative comparison
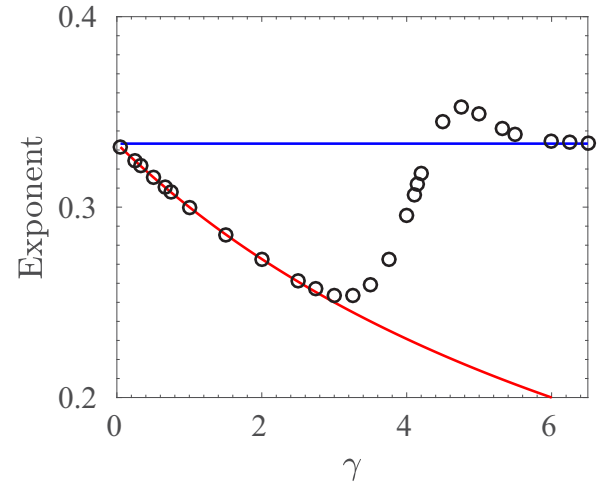

FIG. 4. For $n = 3, d_0 = 8$ Å, $\mathcal{G} = 1$ K/m, $\eta_r = 10^7$, and each γ, a linear least-squares fit is used to obtain a power-law relation, $r_{\max} \propto t^{b(\gamma, \eta_r, d_0, n)}$. Circles represent $b(\gamma, \eta_r, d_0, n)$ from the linear least-squares fit. The lower and upper lines represent the exponents $n/(2n + 3 + \gamma)$ and $n/(2n + 3)$, respectively, corresponding to the similarity solutions (19) and (26).

TABLE I. Numerical and analytical values of γ_{crit} and γ_{sat}.

n	η_r	Numerical		Analytical	
		γ_{crit}	γ_{sat}	γ_{crit}	γ_{sat}
2	10^7	2	4.75	2.09	4.12
3	10^5	1.75	4.75	2.29	4.65
3	10^6	2.25	5.5	2.75	5.58
3	10^7	2.75	6.25	3.21	6.51

between the analytical and numerical results, we compute $\gamma_{\text{crit}}(\eta_r,d_0,n)$ and $\gamma_{\text{sat}}(\eta_r,d_0,n)$ numerically as

$$\gamma_{\text{crit}}(\eta_r,d_0,n) = \max \left\{ \gamma > 0 : \left| b(\gamma,\eta_r,d_0,n) \right. \right.$$
$$\left. \left. - \frac{n}{2n+3+\gamma} \right| \leqslant 10^{-4} \right\}, \qquad (34a)$$

$$\gamma_{\text{sat}}(\eta_r,d_0,n) = \min \left\{ \gamma > 0 : \left| b(\gamma+\delta,\eta_r,d_0,n) \right. \right.$$
$$\left. \left. - \frac{n}{2n+3} \right| \leqslant 10^{-4}, \forall \delta \geqslant 0 \right\}. \qquad (34b)$$

The numerically and analytically determined γ_{crit} and γ_{sat} are shown in Table I for $d_0 = 8\,\text{Å}$: For $n = 3$ and $\eta_r = 10^5, 10^6, 10^7$; and for $n = 2$ and $\eta_r = 10^7$.

Similarity solution for $0 < \gamma \leqslant \gamma_{\text{crit}}(\eta_r,d_0,n)$: We compute the similarity solution, $g_\gamma(\zeta_\gamma)$, numerically by rescaling the deformation, $r(x,t)$, and the position, x, using Eqs. (26) and (27). Figure 5(a) shows the similarity solution $g_2(\zeta_2)$ for $\eta_r = 10^7$.

Breakdown of similarity solution for $\gamma_{\text{crit}}(\eta_r,d_0,n) < \gamma < \gamma_{\text{sat}}(\eta_r,d_0,n)$: For $\eta_r = 10^7$ and $\forall \gamma \in (\gamma_{\text{crit}},\gamma_{\text{sat}})$, we compute both $g_\gamma(\zeta_\gamma)$ and $g(\zeta)$ numerically. We find that none of the functions $g(\zeta)$ and $g_\gamma(\zeta_\gamma)$ exhibits self-similarity. For $\eta_r = 10^7$, we plot $g_{4.75}(\zeta_{4.75})$ in Fig. 5(b) corresponding to the dimensional time 1, 10, and 10^2 h, where the breakdown

of the self-similarity is shown. We have also confirmed that $g(\zeta)$ does not preserve self-similarity (not shown).

Similarity solution for $\gamma \geqslant \gamma_{\text{sat}}(\eta_r,d_0,n)$: As in the case of $0 < \gamma < \gamma_{\text{sat}}(\eta_r,d_0,n)$, we compute $g_\gamma(\zeta_\gamma)$ and $g(\zeta)$ numerically and, as explained in Sec. IV A 1, only $g(\zeta)$ reflects the self-similar behavior of the deformation (not shown).

2. Capillary deformation

Figure 6 shows the dimensional capillary deformation as a function of position at dimensional time 10^2 h for different values of the power-law exponent γ from the three subintervals: (i) $(0,\gamma_{\text{crit}}]$, (ii) $(\gamma_{\text{crit}},\gamma_{\text{sat}})$, and (iii) $[\gamma_{\text{sat}},\infty)$. For $\gamma \in (0,\gamma_{\text{crit}})$, the dynamic viscosity of the liquid is dominated by the proximity effect; the liquid volume flux ($\mathcal{Q}$) is reduced relative to that corresponding to the bulk viscosity model ($\mathcal{Q}_b$) across the entire region from the warm to the cold end. Whence, there is less net solidification and capillary deformation relative to the bulk viscosity model [7] [cf. Figs. 6(a) versus 6(b)]. This is in accordance with the similarity solution $g_\gamma(\zeta_\gamma)$.

For $\gamma_{\text{crit}} < \gamma < \gamma_{\text{sat}}$, the initial solidification and hence capillary deformation in the region $x \leqslant x_{\text{cross}}$ is almost identical for both of the viscosity models, which deviate from each other only in the region $x > x_{\text{cross}}$. In other words, $\mathcal{Q}(t=0) = \mathcal{Q}_b(t=0)$ for $x \leqslant x_{\text{cross}}$ and $\mathcal{Q}(t=0) < \mathcal{Q}_b(t=0)$ for $x > x_{\text{cross}}$. Because the viscosity at the warm end where the film thickness is large remains unaltered relative to the bulk value, so too is the volume flux at the warm end. Therefore, while the thermomolecular pressure gradient depends on the temperature gradient, the gradient in the volume flux depends on the gradient in the film thickness. The latter differs in general between the case with the bulk viscosity [7] and that with the proximity effect. However, this difference only manifests itself when the film gets sufficiently thin to distinguish the differences in viscosities and thus the capillary deformation. Hence, the sudden drop in the volume flux at $x \approx x_{\text{cross}}$ is accompanied by more solidification in the region $x < x_{\text{cross}}$ for any
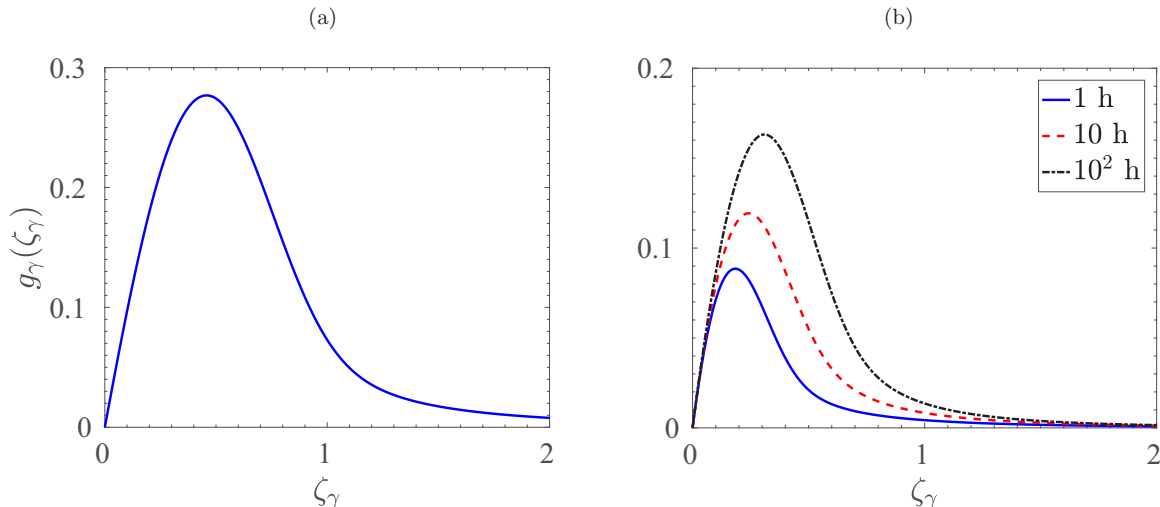
(a)

(b)

FIG. 5. For $\eta_r = 10^7$, the deformation is presented in terms of the similarity variables, viz., Eq. (27): (a) $g_2(\zeta_2)$ is self-similar, but (b) $g_{4.75}(\zeta_{4.75})$ is not self-similar. The legend in the inset corresponds to the time in dimensional units. Note the difference in the vertical scale.
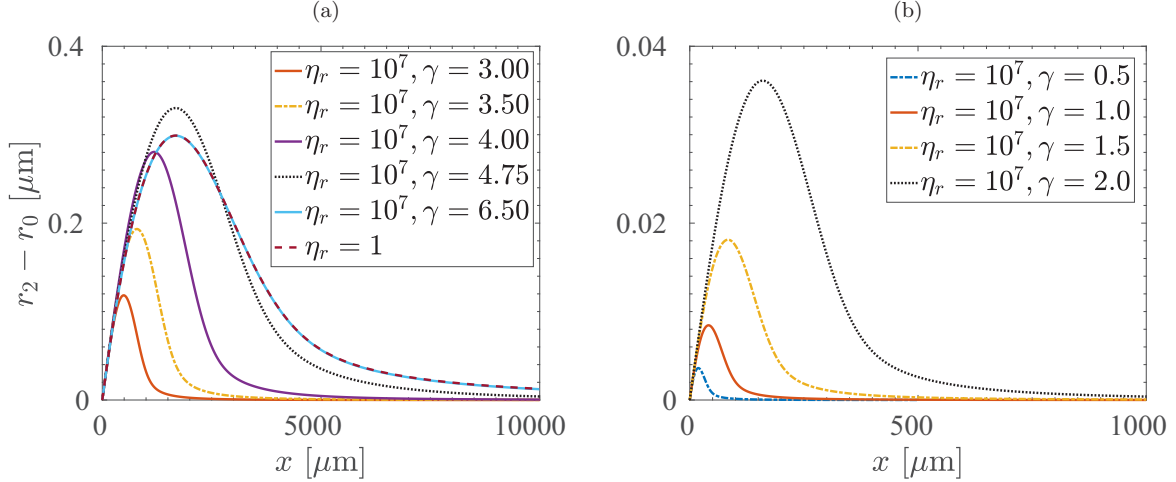
FIG. 6. Dimensional deformation as a function of position at dimensional time 10^2 h for the parameters shown in the insets, and $\mathcal{G} = 1$ K/m, $n = 3$, $d_0 = 8$ Å. Note the difference in the vertical scales.

$\gamma \in (\gamma_{\text{crit}}, \gamma_{\text{sat}})$, when compared to the case of a constant bulk viscosity, or $\gamma \geqslant \gamma_{\text{sat}}$ [see the curves corresponding to $\eta_r = 10^7, \gamma = 4, 4.75, 6.5$, and $\eta_r = 1$ in Fig. 6(a)]. In this process for some γ from the range $(\gamma_{\text{crit}}, \gamma_{\text{sat}})$, we obtain $r_{\max}(T_f; \eta_r \neq 1, \gamma) > r_{\max}(T_f; \eta_r \neq 1, \gamma_{\text{sat}})$ [or $r_{\max}(T_f; \eta_r = 1)$].

Independent of the magnitude of the maximum deformation, $r_{\max}$, we observe a universal behavior in its position, $x_{\max}$. For any d_0, n, λ_n, and η_r, we obtain $x_{\max}(T_f; \gamma_i) < x_{\max}(T_f; \gamma_j)$ for $0 < \gamma_i < \gamma_j \leqslant \gamma_{\text{sat}}$. The gradient of the volume flux, $\partial_x \mathcal{Q}$, for $0 < \gamma < \gamma_{\text{sat}}$, is larger than that for $\gamma \geqslant \gamma_{\text{sat}}$ (or, $\eta_r = 1$), and this gradient decreases as γ increases. In other words, for the same temperature gradient in both cases, the location of the maximum solidification (deformation of the capillary wall) moves toward the warm end as γ decreases. Finally, as seen when comparing Figs. 7 and 6(a), a larger temperature gradient results in a larger deformation that is more highly localized towards higher temperatures.
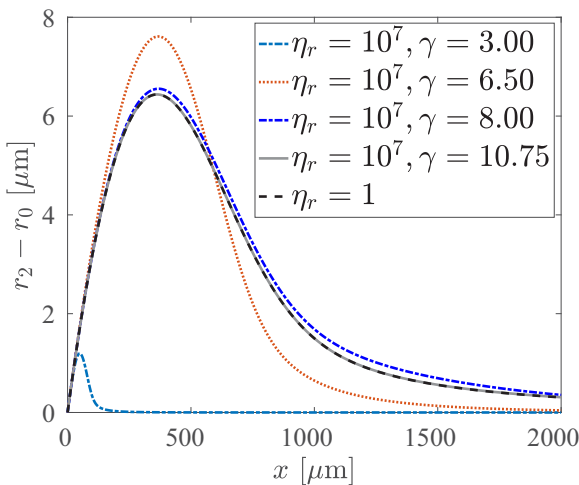
3. $\gamma^{\star}(\eta_r, d_0, n)$

We close this section by computing

$$\gamma^{\star}(\eta_r, d_0, n) = \underset{\gamma}{\arg\max}\ r_{\max}(t = T_f; \gamma, \eta_r, d_0, n), \quad (35)$$

which corresponds to the power-law exponent that is associated with the largest maximum deformation of the capillary wall at T_f for given values of η_r, d_0, and n. Figure 8 shows $\gamma^{\star}$ as a function of η_r for $d_0 = 8$ Å, $n = 3$, and $\mathcal{G} = 1$ K/m. A linear least-squares fit of the numerically computed $\gamma^{\star}$ yields $\gamma^{\star} = 0.8905 + 0.2358 \ln \eta_r$. The shaded region corresponds to the range of γ such that $r_{\max}(T_f; \eta_r > 1) > r_{\max}(T_f; \eta_r = 1)$.

FIG. 7. Same as Fig. 6, but for $\mathcal{G} = 10^2$ K/m, $n = 3$, $d_0 = 8$ Å. Note the difference in the scale of the axes relative to Fig. 6(a).

FIG. 8. For $n = 3, d_0 = 8$ Å, $\mathcal{G} = 1$ K/m, we obtain the relation between $\gamma^{\star}$ and η_r. Symbols are the data points obtained from the numerical solutions. The dash-dotted line represents the linear least-squares fit: $\gamma^{\star} = 0.8905 + 0.2358 \ln \eta_r$. The shaded region corresponds to the range of γ such that $r_{\max}(T_f; \eta_r > 1) > r_{\max}(T_f; \eta_r = 1)$.
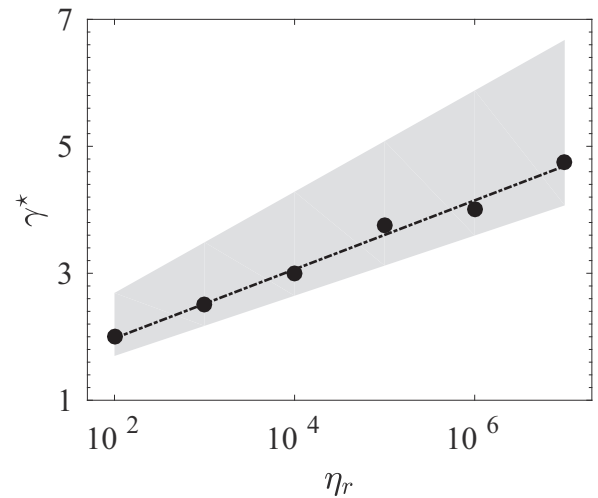
V. CONCLUSIONS

Motivated by a basic question in surface phase transitions, we have developed a phenomenological theory to treat proximity effects in the context of the dynamics of interfacially premelted liquid films. The principal phenomenon capturing our interest is that as the temperature is reduced and surface and interfacially melted films thin, as described by Eq. (2), a solid-like ordering is imprinted upon the liquid and eventually spans its thickness. By parity of reasoning an interface that, upon sufficient increase in temperature, undergoes surface melting is best described as a disordered solid surface, the disorder of which eventually acquires the properties of the bulk liquid. Although we realize that such ordering is not captured by the mean-field theory leading to Eq. (2), that theory nonetheless clearly captures the fact that the thin film is truly a surface phase that would not exist in the absence of the effective field of interactions captured by $\mathcal{I}(d)$ in Eq. (1). There are two obvious approaches one might take to address the ordering. In one, a structurally sensitive surface probe might be employed beginning at very low (high) temperatures and the breakdown (buildup) of ordering as the temperature is increased (decreased) along coexistence could be studied. In the other, which we use here, the dynamical consequences of the ordering effects, through their influence on the viscosity of the interfacially melted film, play out. In the former case there is little quantitative guidance from experiment, and simulations are unable to span the required thermodynamic range (e.g., [19–21] and references therein). In the latter case there is ample evidence from a wide range of materials of the effects of confinement on the dynamical properties, although no such measurements have been made *in-situ* in a premelted liquid film. We thus translated the observed proximity effects on the increase of the dynamic viscosity into the setting that has a firm experimental and theoretical foundation for temperatures very near the bulk melting temperature [5,7,10,11]. This approach provides an ideal comparative setting.

Building upon a range of measurements and materials of the increase in the dynamic viscosity upon confinement, we took the simplest approach in Eq. (5) of a power-law behavior with film thickness controlled by a single exponent γ, whose range in several materials is seen in Fig. 2. The premelted film disjoins its solid phase from a confining elastic capillary tube and the thermomolecular pressure gradient is imposed by setting up a constant temperature gradient parallel to the interface. In the previous study of this system there is no proximity effect and the film viscosity is the bulk value [7]. The central physical results can be seen through the comparison between the results with and without the proximity effect, as seen in Fig. 6(a). We find that, depending on the strength of the increase in viscosity with change in thickness, determined by γ, the dynamics of deformation is quantitatively different. For small γ, the enhanced viscosity is experienced across a larger fraction of the film and as γ increases the ordering decays more rapidly and a larger fraction of the film has bulk behavior.

Hence, for small γ the viscous resistance to flow is substantial and most of the gradient in the volume flux occurs at the largest temperatures where the film is the thickest. However, as the gradient in the volume flux controls the capillary deformation, for small γ the deformation is correspondingly small. As γ increases, so too does the magnitude of the deformation and its position moves away from the entrance to the capillary tube. However, there is a γ beyond which the proximity effect saturates and there is no longer a change in the viscosity with film thickness, after which we recover the previous results [7] where the capillary tube deforms over a larger region because there is no thickness—and hence temperature—dependence of the viscosity controlling the volume flux.

Several interesting mathematical results arise in the context of this model. These principally arise from the influence of the viscosity model on the dynamics. The semi-infinite bulk model admitted similarity solutions [7], but because of the film thickness dependence of viscosity, given by Eq. (5), and the temperature dependence of the film thickness, the value of the decay γ effectively imposed an external length scale on the problem, which can compromise the similarity behavior, as captured by Fig. 4. The interplay between the nature of the interactions driving the interfacial melting, captured by n, and the viscosity decay, captured by γ, sets the stage for the existence of similarity solutions.

Finally, the processes discussed here, and in our previous work [5,10], have implications for frost heave in a wide variety of situations, including biological, geological, and technological settings, such as the freezing of soils, cells and tissues, cancer treatment, food science, fish biology, and botany. In particular, phase changes and the ordering of water in membranes are active areas of research, e.g., [36], and our results show that even if the temperature is very low or the pores of a system are highly restrictive, the same basic flow driving deformation persists. So long as there is a temperature gradient, the thermomolecular pressure gradient will eventually build up a deformation near the bulk melting temperature that may be sufficient for rupture of the confining body, e.g., [37] and references therein. As the proximity effect restricts motion of unfrozen liquid at lower temperatures the deformation will be more highly localized at higher temperatures, as seen by comparing Figs. 6(a) and 7. Both the magnitude of the deformation and its position relative to the bulk melting temperature provide experimental targets to indirectly extract constraints, such as the value of γ, on the proximity effect. It is hoped that such experiments will be performed.

TABLE II. $n = 3, \lambda_n = 5.3947$ Å, $d_0 = 8$ Å, $\eta_r = 10^5, \mathcal{G} = 1$ K/m.

γ	$(r_2 - r_0)_{\max}(T_f)$ (μm)	$x_{\max}$ (μm)
2.75	0.2546	1.1250×10^3
3	0.2918	1.3500×10^3
3.05	0.2974	1.4000×10^3
3.1	0.3023	1.4250×10^3
3.75	0.3113	1.6750×10^3
4	0.3058	1.7000×10^3
4.15	0.3034	1.7000×10^3
4.75	0.2995	1.6750×10^3
5	0.2991	1.6750×10^3
5.25	0.2989	1.6750×10^3

APPENDIX: PARAMETERS

Parameters are given below for the ice-water system as found in Ref. [8], except for the temperature gradient, which is about 100 times weaker here.

$$\mathcal{G} = 1 \text{ K/m}, \tag{A1a}$$

$$k = 3 \times 10^9 \text{ Pa/m}, \tag{A1b}$$

$$\rho_l = 10^3 \text{ kg/m}^3, \tag{A1c}$$

$$\rho_s = 0.9167 \times 10^3 \text{ kg/m}^3, \tag{A1d}$$

$$T_m = 273.16 \text{ K}, \tag{A1e}$$

$$\eta_b = 1.307 \times 10^{-3} \text{ kg/ms}, \tag{A1f}$$

$$\lambda^3 = \Lambda = 1.57 \times 10^{-28} \text{ m}^3, \tag{A1g}$$

$$q_m = 334 \times 10^3 \text{ J/kg}. \tag{A1h}$$

Parameters used in the numerical solutions are given in Tables II–VI.

TABLE III. $n = 3, \lambda_n = 5.3947$ Å, $d_0 = 8$ Å, $\eta_r = 10^6, \mathcal{G} = 1$ K/m.

γ	$(r_2 - r_0)_{\max}(T_f)$ (μm)	$x_{\max}$ (μm)
3.25	0.2466	1.0500×10^3
3.55	0.2943	1.3000×10^3
3.575	0.2975	1.3250×10^3
3.625	0.3034	1.3750×10^3
4	0.3241	1.6000×10^3
4.25	0.3198	1.6750×10^3
4.5	0.3116	1.7000×10^3
4.8	0.3046	1.7000×10^3
5	0.3020	1.7000×10^3
5.5	0.2994	1.6750×10^3
5.75	0.2991	1.6750×10^3
6	0.2989	1.6750×10^3

TABLE IV. $n = 3, \lambda_n = 5.3947$ Å, $d_0 = 8$ Å, $\eta_r = 10^7, \mathcal{G} = 1$ K/m.

γ	$(r_2 - r_0)_{\max}(T_f)$ (μm)	$x_{\max}$ (μm)
0.25	0.0023	0.1225×10^2
0.33	0.0027	0.1425×10^2
0.5	0.0036	0.1875×10^2
0.67	0.0048	0.2450×10^2
0.75	0.0056	0.2800×10^2
1	0.0084	0.4100×10^2
1.5	0.0184	0.8500×10^2
2	0.0361	0.1600×10^3
2.5	0.0674	0.2875×10^3
3	0.1184	0.5000×10^3
3.5	0.1934	0.8000×10^3
4	0.2805	1.1750×10^3
4.1	0.2956	1.2750×10^3
4.15	0.3024	1.3000×10^3
4.2	0.3086	1.3500×10^3
4.75	0.3302	1.6750×10^3
5	0.3204	1.7250×10^3
5.325	0.3086	1.7000×10^3
6	0.3000	1.6750×10^3
6.5	0.2990	1.6750×10^3
6.25	0.2993	1.6750×10^3

TABLE V. $n = 3, \lambda_n = 5.3947$ Å, $d_0 = 8$ Å, $\eta_r = 10^7, \mathcal{G} = 10^2$ K/m.

γ	$(r_2 - r_0)_{\max}(T_f)$ (μm)	$x_{\max}$ (μm)
3	1.1941	0.495×10^2
6.5	7.6105	0.370×10^3
8	6.5530	0.370×10^3
9	6.4494	0.365×10^3
9.5	6.4411	0.365×10^3
10.25	6.4380	0.360×10^3
10.75	6.4375	0.360×10^3
11	6.4375	0.360×10^3

TABLE VI. $n = 2, \lambda_n = 5.3947$ Å, $d_0 = 8$ Å, $\eta_r = 10^7, \mathcal{G} = 1$ K/m.

γ	$(r_2 - r_0)_{\max}(T_f)$ (μm)	$x_{\max}$ (μm)
0.05	0.0239	0.110×10^3
0.5	0.0598	0.250×10^3
1	0.1456	0.600×10^3
1.5	0.3175	1.250×10^3
2	0.6314	2.425×10^3
2.1	0.7173	2.700×10^3
2.25	0.8623	3.300×10^3
2.5	1.1500	4.300×10^3
2.75	1.4867	5.600×10^3
3	1.8372	6.975×10^3
3.25	2.1221	8.400×10^3
3.5	2.2547	9.400×10^3
3.75	2.2459	9.900×10^3
4	2.1975	1.000×10^4
4.25	2.1667	1.000×10^4
4.5	2.1535	9.900×10^3
4.75	2.1486	9.900×10^3
5	2.1469	9.900×10^3

[1] M. Schick, in *Les Houches Session XLVIII* (Elsevier, Amsterdam, 1990), pp. 415–497.

[2] S. A. Safran, *Statistical Thermodynamics of Surfaces, Interfaces, and Membranes* (Addison-Wesley, Reading, MA, 1994).

[3] R. H. French, V. A. Parsegian, R. Podgornik, R. F. Rajter, A. Jagota, J. Luo, D. Asthagiri, M. K. Chaudhury, Y.-m. Chiang, S. Granick, S. Kalinin, M. Kardar, R. Kjellander, D. C. Langreth, J. Lewis, S. Lustig, D. Wesolowski, J. S. Wettlaufer, W.-Y. Ching, M. Finnis, F. Houlihan, O. A. von Lilienfeld, C. J. van Oss, and T. Zemb, Rev. Mod. Phys. **82**, 1887 (2010).

[4] J. N. Israelachvili, *Intermolecular and Surface Forces*, 3rd ed. (Academic Press, New York, 2011).

[5] J. G. Dash, A. W. Rempel, and J. S. Wettlaufer, Rev. Mod. Phys. **78**, 695 (2006).

[6] L. A. Wilen, J. S. Wettlaufer, M. Elbaum, and M. Schick, Phys. Rev. B **52**, 12426 (1995).

[7] J. S. Wettlaufer and M. G. Worster, Phys. Rev. E **51**, 4679 (1995).

[8] J. S. Wettlaufer, M. G. Worster, L. A. Wilen, and J. G. Dash, Phys. Rev. Lett. **76**, 3602 (1996).

[9] P. G. de Gennes, Rev. Mod. Phys. **57**, 827 (1985).

[10] J. S. Wettlaufer and M. G. Worster, Annu. Rev. Fluid Mech. **38**, 427 (2006).

[11] L. A. Wilen and J. G. Dash, Phys. Rev. Lett. **74**, 5076 (1995).

[12] A. W. Rempel, J. S. Wettlaufer, and M. G. Worster, J. Fluid Mech. **498**, 227 (2004).

[13] D.-M. Zhu, O. E. Vilches, J. G. Dash, B. Sing, and J. S. Wettlaufer, Phys. Rev. Lett. **85**, 4908 (2000).

[14] S. Taber, J. Geol. **37**, 428 (1929).

[15] T. Mizusaki and M. Hiroi, Physica B (Amsterdam) **210**, 403 (1995).

[16] R. Evans, J. Phys.: Condens. Matter **2**, 8989 (1990).

[17] H. K. Christenson, J. Phys.: Condens. Matter **13**, R95 (2001).

[18] J. Koplik and J. R. Banavar, Annu. Rev. Fluid Mech. **27**, 257 (1995).

[19] H. Nada and Y. Furukawa, J. Phys. Chem. B **101**, 6163 (1997).

[20] H. Nada and Y. Furukawa, Surf. Sci. **446**, 1 (2000).

[21] H. Nada, J. Chem. Phys. **145**, 244706 (2016).

[22] B. Pittenger, S. C. Fain, M. J. Cochran, J. M. K. Donev, B. E. Robertson, A. Szuchmacher, and R. M. Overney, Phys. Rev. B **63**, 134102 (2001).

[23] A. Döppenschmidt, M. Kappl, and H.-J. Butt, J. Phys. Chem. B **102**, 7813 (1998).

[24] J. G. Dash, Scr. Mater. **49**, 1003 (2003).

[25] A. Dhinojwala and S. Granick, J. Am. Chem. Soc. **119**, 241 (1997).

[26] R. C. Major, J. E. Houston, M. J. McGrath, J. I. Siepmann, and X.-Y. Zhu, Phys. Rev. Lett. **96**, 177803 (2006).

[27] L. Bureau, Phys. Rev. Lett. **104**, 218302 (2010).

[28] U. Raviv and J. Klein, Science **297**, 1540 (2002).

[29] S. Granick, Science **253**, 1374 (1991).

[30] Y. Zhu and S. Granick, Langmuir **19**, 8148 (2003).

[31] Y. Zhu and S. Granick, Phys. Rev. Lett. **93**, 096101 (2004).

[32] T. Becker and F. Mugele, Phys. Rev. Lett. **91**, 166104 (2003).

[33] R. LeVeque, *Finite Difference Methods for Ordinary and Partial Differential Equations* (SIAM, New York, 2007).

[34] S. Toppaladoddi and J. S. Wettlaufer, J. Stat. Phys. **167**, 683 (2017).

[35] See Supplemental Material at http://link.aps.org/supplemental/10.1103/PhysRevE.96.052801 for the numerical scheme and additional range of γ explored, but not shown here.

[36] V. A. Parsegian, *Van der Waals Forces: A Handbook for Biologists, Chemists, Engineers, and Physicists* (Cambridge University Press, New York, 2005).

[37] I. Vlahou and M. G. Worster, J. Glaciol. **56**, 271 (2010).